ORIGINAL ARTICLE

Standard SPECT myocardial perfusion estimation from half-time acquisitions using deep convolutional residual neural networks

Isaac Shiri, MSc,[a] Kiarash AmirMozafari Sabet, MSc,[b] Hossein Arabi, PhD,[a] Mozhgan Pourkeshavarz, MSc,[c,d] Behnoosh Teimourian, PhD,[e] Mohammad Reza Ay, PhD,[e,f] and Habib Zaidi, PhD[a,g,h,i]

[a] Division of Nuclear Medicine and Molecular Imaging, Geneva University Hospital, Geneva 4, Switzerland
[b] School of Electrical Engineering, Sharif University of Technology, Tehran, Iran
[c] Rajaie Cardiovascular Medical and Research Center, Iran University of Medical Science, Tehran, Iran
[d] Department of Computer Engineering, Shahid Beheshti University, Tehran, Iran
[e] Research Center for Molecular and Cellular Imaging, Tehran University of Medical Sciences, Tehran, Iran
[f] Department of Medical Physics and Biomedical Engineering, Tehran University of Medical Sciences, Tehran, Iran
[g] Geneva University Neurocenter, Geneva University, Geneva, Switzerland
[h] Department of Nuclear Medicine and Molecular Imaging, University of Groningen, University Medical Center Groningen, Groningen, The Netherlands
[i] Department of Nuclear Medicine, University of Southern Denmark, Odense, Denmark

Received Dec 19, 2019; accepted Mar 26, 2020
doi:10.1007/s12350-020-02119-y

Introduction. **The purpose of this work was to assess the feasibility of acquisition time reduction in MPI-SPECT imaging using deep leering techniques through two main approaches, namely reduction of the acquisition time per projection and reduction of the number of angular projections.**

Methods. **SPECT imaging was performed using a fixed 90° angle dedicated dual-head cardiac SPECT camera. This study included a prospective cohort of 363 patients with various clinical indications (normal, ischemia, and infarct) referred for MPI-SPECT. For each patient, 32 projections for 20 seconds per projection were acquired using a step and shoot protocol from the right anterior oblique to the left posterior oblique view. SPECT projection data were reconstructed using the OSEM algorithm (6 iterations, 4 subsets, Butterworth post-reconstruction filter). For each patient, four different datasets were generated, namely full time (20 seconds) projections (FT), half-time (10 seconds) acquisition per projection (HT), 32 full projections (FP), and 16 half projections (HP). The image-to-image transformation via the residual network was implemented to predict FT from HT and predict FP from HP images in the projection domain. Qualitative and quantitative evaluations of the proposed framework was performed using a tenfold cross validation scheme using the root mean square error (RMSE),**

Electronic supplementary material The online version of this article (https://doi.org/10.1007/s12350-020-02119-y) contains supplementary material, which is available to authorized users.

The authors of this article have provided a PowerPoint file, available for download at SpringerLink, which summarises the contents of the paper and is free for re-use at meetings and presentations. Search for the article DOI on SpringerLink.com.

Reprint requests: Habib Zaidi, PhD, Division of Nuclear Medicine and Molecular Imaging, Geneva University Hospital, 1211 Geneva 4, Switzerland; *habib.zaidi@hcuge.ch*

1071-3581/$34.00

absolute relative error (ARE), structural similarity index, peak signal-to-noise ratio (PSNR) metrics, and clinical quantitative parameters.

Results. **The results demonstrated that the predicted FT had better image quality than the predicted FP images. Among the generated images, predicted FT images resulted in the lowest error metrics (RMSE = 6.8 ± 2.7, ARE = 3.1 ± 1.1%) and highest similarity index and signal-to-noise ratio (SSIM = 0.97 ± 1.1, PSNR = 36.0 ± 1.4). The highest error metrics (RMSE = 32.8 ± 12.8, ARE = 16.2 ± 4.9%) and the lowest similarity and signal-to-noise ratio (SSIM = 0.93 ± 2.6, PSNR = 31.7 ± 2.9) were observed for HT images. The RMSE decreased significantly (*P* value < .05) for predicted FT (8.0 ± 3.6) relative to predicted FP (6.8 ± 2.7).**

Conclusion. **Reducing the acquisition time per projection significantly increased the error metrics. The deep neural network effectively recovers image quality and reduces bias in quantification metrics. Further research should be undertaken to explore the impact of time reduction in gated MPI-SPECT. (J Nucl Cardiol 2021;28:2761–79.)**

Key Words: SPECT • myocardial perfusion imaging • deep learning • short acquisition

Abbreviations

SPECT	Single-photon emission computed tomography
MPI	Myocardial perfusion imaging
CAD	Coronary artery disease
CNN	Convolutional neural network
ResNet	Residual network
FT-FP	Full time and full projection, reference images
HP	Half projection
HT	Half time
FP-Prediction	Full projection prediction
FT-Prediction	Full time prediction

See related editorial, pp. 2780–2783

INTRODUCTION

Myocardial perfusion imaging (MPI) using single-photon emission computed tomography (SPECT) plays a pivotal role in prediction, diagnosis and prognosis of coronary artery disease (CAD).[1] There is a pressing demand to shortening the acquisition time of MPI-SPECT to enhance patient's comfort, reduce examination costs through higher patient throughput, and reduce the likelihood of patient motion.[2,3] However, reducing the acquisition time amplifies noise, thus hampering clinical interpretation of SPECT images. Recent advances in hardware (novel cameras and collimators) and software (reconstruction algorithms incorporating noise regularization and resolution recovery) facilitate the possibility of reducing scanning time and/or injected activity without degrading image quality.[3-5]

Recent efforts focused on investigating the potential of new acquisition and reconstruction protocols involving the use of low-energy high-resolution collimators, multifocal collimators, such as IQ SPECT,[6] and dedicated reconstruction algorithms[7] on the reduction of administered activity and acquisition time for MPI imaging. In this regard, a wide-beam reconstruction algorithm was proposed for quarter-time (1/4th) MPI-SPECT imaging,[8] though this approach faces major challenges in ECG-gated imaging and overweight patients.

Recent developments in machine/deep learning have successfully introduced a paradigm shift in medical image analysis techniques. A number of studies have assessed the relevance of machine/deep learning in various areas of medical image analysis including disease classification,[9,10] image denoising,[11] resolution recovery,[12] image reconstruction,[13] segmentation,[14,15] and PET attenuation correction.[16,17]

Ma et al.[18] used a convolutional neural network (CNN) in the diagnosis of different thyroid diseases (Graves' disease, Hashimoto disease, and subacute thyroiditis) using SPECT images. They demonstrated that their proposed method is efficient for SPECT imaging-based classification of thyroid diseases. Betancur et al.[19] performed a study for automatic obstructive disease prediction from MPI-SPECT images using a deep CNN, reporting improved prediction of per-patient and per-vessel coronary artery disease. A more recent multi-centric study showed that a deep CNN improves obstructive coronary artery disease prediction from upright-supine MPI-SPECT compared with current quantitative techniques.[20] Another study performed by Wang et al.[21] reported on the feasibility of deep learning-based (using a V-net architecture) automatic segmentation and quantification of the left ventricle from gated MPI-SPECT images.

Dietze et al.[22] used a deep CNN to enhance fast filtered backprojection reconstructed SPECT images to achieve a quality comparable to Monte Carlo-based reconstructions. They reported that CNN enabled generation of SPECT images with a quality similar to that

obtained with Monte Carlo-based reconstruction within seconds. Ramon et al.[23] reported on a feasibility study for denoising low-dose MPI-SPECT imaging using 3D convolutional auto-encoders to produce standard full dose images from 1/8th and 1/16th dose images. They reported improvements in image quality comparable to conventional noise reduction methods. More recently, the same group used a 3D deep residual CNN to generate standard full dose images from ¼ dose MPI-SPECT images.[24] The proposed approach led to effective noise reduction in the myocardium, outperforming conventional post-processing methods, such as spatiotemporal non-local means filtering.

There are fundamental differences between fast (half-projection) and low-dose (half-time) scans although the final impact on total acquisition time is the same. Half-projection acquisition only reduces patient scanning time and reduces the number of projection samples without impacting the injected activity and hence the radiation dose to the patient. Conversely, a half-time scan mimics both a low-dose scan (due to the reduced number of counts) and fast acquisition with standard injected activity (due to reduced scan time). In this work, we set out to investigate both options with the aim to optimize cardiac SPECT protocols.

The purpose of this work is to explore the possibility of time reduction in cardiac MPI-SPECT imaging using two main approaches, namely (i) reducing the scanning time per projection (half time) and (ii) reducing the number of acquired projections during image acquisition.

MATERIALS AND METHODS

Image Acquisition

MPI-SPECT imaging was performed on fixed 90° angle dual-head ProSPECT dedicated cardiac SPECT camera.[25] The ProSPECT detector is composed of Thallium-activated Sodium Iodide (NaI(Tl)) crystal having a size of 40×25 cm^2 and 9.5 mm thickness. A square array of PMTs (24 pcs, 76×76 mm) was optically coupled to a 20-mm thick fused-quartz light-guide using a silicon-based curing compound as optical glue. Intrinsic and extrinsic spatial resolutions with low-energy high-resolution collimator (LEHR, 35 mm thickness) at 10 cm from the surface of the detector was 3.7 mm and 7.5 mm, respectively. The energy resolution and sensitivity were 9.5% and 5.19 cpm/kBq, respectively.[25]

This prospective study included a cohort of 363 patients with different clinical indications (normal, ischemia, and infarct) referred for MPI-SPECT imaging. Gated MPI-SPECT stress imaging was preformed 45-60 min after intravenous administration of 555-925 MBq of ^{99m}Tc-sestamibi. List-mode electrocardiogram (ECG)-gated MPI-SPECT data were acquired using 16 frames per cardiac cycle and 30% acceptance window for R–R interval length using forward–backward gating method. A step and shoot acquisition protocol consisting of 32 projections with 20 seconds per projection from the right anterior oblique (RAO) to the left posterior oblique (LPO) view was used.

Data Processing

Half time (HT) For each patient, two set of projections were generated from the full acquisition list mode data, the whole acquisition (20 seconds per projection) was considered as full time (FT) projection data while the first 10 seconds of the list mode data were used to create half time (HT) projections.

Half projection (HP) Half projection (HP, 16 projections) data set were obtained by excluding even projections from full time acquisition (32 projections, 20 seconds) projections.

Deep Learning Algorithm

Network architecture The image-to-image transformation was performed using a deep residual neural network (ResNet)[26] for FT and FP projection prediction. ResNet is composed of 20 convolutional layers where a convolution kernel with 3×3 voxels is used with zero dilatation for the first seven layers (low-level features extraction), the next seven layers with a dilated convolution kernel by a factor of two (medium-level features extraction) and the last six layer with a dilation by a factor four (high level feature extraction). Every two convolutional layers linked with residual connection and leaky rectified linear unit (LReLU) was used for activation function. The residual network (ResNet) [26] implemented in Python libraries of Niftynet pipeline,[27] built upon TensorFlow (version 1.12.1)[28] was utilized to predict FT and FP projections from HT and HP projections, respectively.

To avoid a large number of trainable parameters, a kernel of 3×3 was chosen for all convolutions. Many architectures down-sample the intermediate feature maps to capture large image contexts at the cost of reduced spatial resolution. Thus, up-sampling convolutional layers are employed to partially recover the lost resolution, which also adds to the computational burden/cost of the model. The advantages of dilated convolutions are that features are extracted from high resolution inputs while any receptive field (in terms of size) can be chosen. Instead of a down-sampling/up-sampling pipeline, the ResNet architecture adopts dilated convolution with factors of 2 and 4 for seven intermediate and six last layers to ensure effective feature extraction (Figure 1a). It should be noted that the dilated convolutions contain the same number of free (trainable) parameters compared to conventional kernels. The key feature of ResNet, in addition to dilated convolution kernels, is residual connections which bypass the parameterized layers. This is performed through combining (by addition) the input and output of a block to render a smooth information propagation and enhance the training speed/quality. The ResNet architecture benefits from 9 residual blocks

(Figure 1a), which results in a large number of receptive fields (which improves the process of feature extraction).

Implementation details The training for FT prediction was performed using 11616 (363 × 32) pairs of HT and FT projections as input/output, respectively. To this end, the ResNet model with a 2D spatial window equal to 64 × 64 voxels and batch size of 30 were used. The training for FP prediction was performed using 5445 (363 × 15) projection pairs. Two projections (left and right neighbors of the target projection) were used as input to the network to predict the intermediate projection. The same setting was used for the training of the two networks (FT and FP predictions) as follows: learning rate = 0.001, sample per volume = 1, optimizer = Adam, loss function = L2norm and decay = 0.0001. The implementation of network input and target in FT and FP predictions are presented in Figure 1b.

The optimization of the network was carried out based on the L2 loss function. Though the L1 norm or mean absolute error (MAE) are frequently used in the literature, the L2 loss function exhibited overall better performance for this task. It should be noted that the L2 loss function led to somewhat blurred output compared to L1 and MAE loss functions. However, quantitative parameters demonstrated overall superior performance of the L2 loss function.

Considering a batch size of 30, the training of the network for either FP or FT prediction took about 10 h using a 2080TI GPU, Intel(R) Xeon 2.30 GHz 7i CUP and 64.0 GB RAM. After 10 epochs, the training loss reached its plateau. In the inference phase, the prediction of FP and FT projections took few milliseconds per subject.

Image Reconstruction

The SPECT projection data were reconstructed using OSEM algorithm. The numbers of iterations and subsets were set to 6 and 4, respectively. SPECT reconstruction was repeated five times for each patient to generate FT-FP, HP, HT, predicted FT and predicted FP SPECT images. All images were reconstructed into a 64 × 64 matrix with a voxel size of 6.4 × 6.4 × 6.4 mm. The Butterworth post-reconstruction filter with order = 10 and cut-off = 0.37 was applied to smooth the images.

Qualitative and Quantitative Evaluation

Qualitative and quantitative evaluation of the proposed framework was performed using a tenfold cross validation scheme on 363 subjects. Quantitative evaluation of the predicted images was performed in both image and projection domains. In the projection domain, three datasets (HT, predicted FT, predicted FP) were evaluated against the reference projections obtained from the FT/FP scans. In the image domain, four SPECT images (HT, HP, predicted FT, predicted FP) were compared to reference FT/FP images reconstructed from the full acquisition. The quality of SPECT images was assessed using the following metrics considering SPECT images derived from the full time (20 seconds) and full projection (32 projections) acquisition as reference.

Voxelwise mean error (ME), mean absolute error (MAE), relative error (RE%) and absolute relative error (ARE%) were calculated between reference FT/FP and predicted SPECT images in the projection and image domains.

$$\mathrm{ME} = \frac{1}{vxl}\sum_{v=1}^{vxl} \mathrm{SPECT}_{\mathrm{Predicted}}(v) - \mathrm{SPECT}_{\mathrm{FT-FP}}(v), \quad (1)$$

$$\mathrm{MAE} = \frac{1}{vxl}\sum_{v=1}^{vxl} \left|\mathrm{SPECT}_{\mathrm{predicted}}(v) - \mathrm{SPECT}_{\mathrm{FT-FP}}(v)\right|, \quad (2)$$

$$\mathrm{RE}(\%) = \frac{1}{vxl}\sum_{v=1}^{vxl} \frac{\left(\mathrm{SPECT}_{\mathrm{predicted}}\right)_v - \left(\mathrm{SPECT}_{\mathrm{FT-FP}}\right)_v}{\left(\mathrm{SPECT}_{\mathrm{FT-FP}}\right)_v} \times 100\%, \quad (3)$$

$$\mathrm{ARE}(\%) = \frac{1}{vxl}\sum_{v=1}^{vxl} \left|\frac{\left(\mathrm{SPECT}_{\mathrm{predicted}}\right)_v - \left(\mathrm{SPECT}_{\mathrm{FT-FP}}\right)_v}{\left(\mathrm{SPECT}_{\mathrm{FT-FP}}\right)_v}\right| \times 100\%. \quad (4)$$

Here, $\mathrm{SPECT}_{\mathrm{predicted}}$ stands for SPECT images generated from HT and HP acquisitions, whereas $\mathrm{SPECT}_{\mathrm{FT\text{-}FP}}$ stands for the reference FT-FP SPECT images. vxl and v denote the total number of voxels and voxel index, respectively.

Moreover, the root mean square error (RMSE), structural similarity index (SSIM) and peak signal-to-noise ratio (PSNR) were calculated to assess the quality of the predicted SPECT images

$$\mathrm{RMSE} = \sqrt{\frac{1}{vxl}\sum_{v=1}^{vxl} \left(\mathrm{SPECT}_{\mathrm{predicted}}(i) - \mathrm{SPECT}_{\mathrm{FT-FP}}(i)\right)^2}, \quad (5)$$

$$\mathrm{PSNR(dB)} = 10\log_{10}\left(\frac{\mathrm{Peak}^2}{\mathrm{MSE}}\right), \quad (6)$$

$$\mathrm{SSIM} = \frac{\left(2\mathrm{Ave}_{\mathrm{FT-FP}}\mathrm{Ave}_{\mathrm{predicted}} + C_1\right)\left(2\delta_{\mathrm{ref,predicted}} + C_2\right)}{\left(\mathrm{Ave}^2_{\mathrm{FT-FP}} + Ave^2_{\mathrm{predicted}} + C_1\right)\left(\delta^2_{\mathrm{ref}} + \delta^2_{\mathrm{predicted}} + C_2\right)}. \quad (7)$$

In Eq. (6), Peak denotes the maximum intensity of either $\mathrm{SPECT}_{\mathrm{FT\text{-}FP}}$ or $\mathrm{SPECT}_{\mathrm{predicted}}$, whereas MSE indicates the mean squared error. In Eq. (7), $\mathrm{Ave}_{\mathrm{FT\text{-}FP}}$ and $\mathrm{Ave}_{\mathrm{predicted}}$ stand for the mean value of $\mathrm{SPECT}_{\mathrm{FT\text{-}FP}}$ and $\mathrm{SPECT}_{\mathrm{predicted}}$, respectively. $\delta_{\mathrm{FT\text{-}FP}}$ and $\delta_{\mathrm{predicted}}$ denote the variances and $\delta_{\mathrm{FT\text{-}FP,predicted}}$ the covariances of $\mathrm{SPECT}_{\mathrm{FT\text{-}FP}}$ and $\mathrm{SPECT}_{\mathrm{predicted}}$ images, respectively. The constants (C_1= 0.01 and C_2= 0.02) were set to avoid division by very small values.

Paired-sample *t*-test was used for statistical analysis to compare the image-derived metrics between the generated data sets in the projection and image domains. The significance

level of *P*-value was set to .05 for all comparisons and calculated metrics. Moreover, the voxelwise joint histograms with Pearson correlation were computed to explore the correlation between the generated SPECT images with respect to reference FT-FP images (only in the reconstruction domain).

Quantitative Clinical Evaluation

For clinical evaluation, quantitative parameters were calculated using the non-grated stress SPECT images for HT, HP, predicted FT, predicted FP, and reference FP/FT images using Cedars-Sinai software. These quantitative parameters include Defect, Extent, Summed Stress Percent (SS%), Summed Stress Score (SSS), Total Perfusion Deficit (TPD%), Volume, Wall, Shape Eccentricity and Shape Index. Descriptive statistics of quantitative stress perfusion along with Pearson correlation analysis with respect to reference images were reported.

Further evaluation was performed using Bland–Altman analysis where tbe mean bias, standard deviation, lower and upper bound with 95% confidence interval (CI) as well as repeatability coefficient ($RC = 1.96\sqrt{2\sigma_w^2}$, σ_w is variance) were reported for clinical quantitative parameters.

RESULTS

Projection Domain Analysis

Table 1 summarizes the results of statistical analysis of image quality metrics (mean ± SD), including ME, MAE, voxelwise RE (%), voxelwise ARE (%), SSIM, PSNR, RMSE. The voxelwise RMSEs were 68.4 ± 3.8, 16.4 ± 3.2 and 11.7 ± 2.9 for HT, predicted FP and predicted FT, respectively. The HT projections presented the highest RE (-23.1 ± 4.6%) with respect to the FT projections, whereas the predicted FT and predicted FP projections resulted in RE of 0.4 ± 4.1 and − 2.9 ± 4.8 with respect to FT/FP projections, respectively. The HT projections, predicted FT and predicted FP projections led to SSIM of 0.92 ± 1.4, 0.96 ± 1.2 and 0.94 ± 1.5 and PSNR of 31.9 ± 1.6, 35.6 ± 1.8 and 34.9 ± 1.9, respectively. Overall, the predicted FT projections provided better image quality compared to predicted FP (*P*-value < .05).

Image Domain Analysis

Figure 2 depicts a representative clinical example comparing FT/FP, HT, HP, predicted FT and predicted FP images as well as relative difference maps with respect to reference FT/FP images. The predicted FT and predicted FP images provide good image quality. However, the HT and HP images showed high bias maps with respect to the reference FT/FP images. The predicted FT method provided overly better image quality compared to the predicted FP methods. The line profiles drawn through the myocardium between reference FT/FP images and the predicted FT, predicted FP, HP and HT images are shown in Figure 2. The profiles drawn through the FT/FP and predicted FT images are in very good agreement in low and high-count areas of the myocardium. Figures 3 and 4 show representative reconstructed SPECT images from the predicted FP and predicted FT projections as well as FT/FP images.

Table 2 summarizes the results of statistical analysis of image quality metrics (mean ± SD), including ME, MAE, voxelwise RE, voxelwise ARE, SSIM, PSNR, and RMSE between the different SPECT images. The voxelwise RMSE in reconstructed SPECT images was 16.2 ± 4.9, 4.8 ± 1.7, 3.6 ± 1.3 and 3.1 ± 1.1 for HT, HP, predicted FP and predicted FT, respectively. The HP images showed the lowest RE (0.1 ± 1.3%) compared to HT images (-16.2 ± 4.9%) (*P*-value < .001). The predicted FT and predicted FP images resulted in MAE of 4.8 ± 1.8 and 5.6 ± 2.3 (*P*-value < 0.05) and RE of − 0.2 ± 0.7% and − 0.1 ± 1.0% with respect to the FT/FP images. The HT, HP, predicted FP, and predicted FT led to SSIM of 0.93 ± 1.3, 0.96 ± 1.2, 0.97 ± 1.1 and 0.98 ± 1.1 and PSNR of 32.2 ± 1.5, 35.7 ± 1.5, 36.8 ± 1.5 and 36.0 ± 1.4, respectively. The reconstructed images from predicted FT provided better image quality compared to the predicted FP methods (*P*-value < .05).

Figure 5 shows box plots of MAE, RMSE and ARE (%) comparing various prediction methods. The lowest error was achieved by predicted FT images. The MAE, RMSE, ARE (%) for all patients are presented in Supplemental Figures 1-3. The voxelwise joint histogram analysis of SPECT images (Figure 6) revealed high correlations between FT/FP and predicted FT and predicted FP images (R^2 = 0.983 and 0.987 for predicted FT and predicted FP, respectively).

Clinical Quantitative Evaluation

Tables 3 and 4 summarize the results of the statistical analysis as well as Pearson correlation coefficients (R^2) for the clinical MPI-SPECT studies. Considering the TPD (%) index, SPECT images reconstructed from the predicted FP (18.52 ± 6.00) and predicted FT (18.40 ± 6.00) exhibited close agreement with the reference FT-FP images (TPD = 18.84 ± 6.08%). Likewise, HP and HT images exhibited TPD (%) indices of 17.02 ± 4.98% and 16.49 ± 4.74%, respectively. Table 4 confirms the trend observed in Table 3 wherein Pearson correlation coefficients (R^2) of 0.999, 0.996, 0.930 and 0.837 were observed for predicted FT, predicted FP, HP, and HT with respect to FT-FP images. Moreover, the box plots of TPD (%),

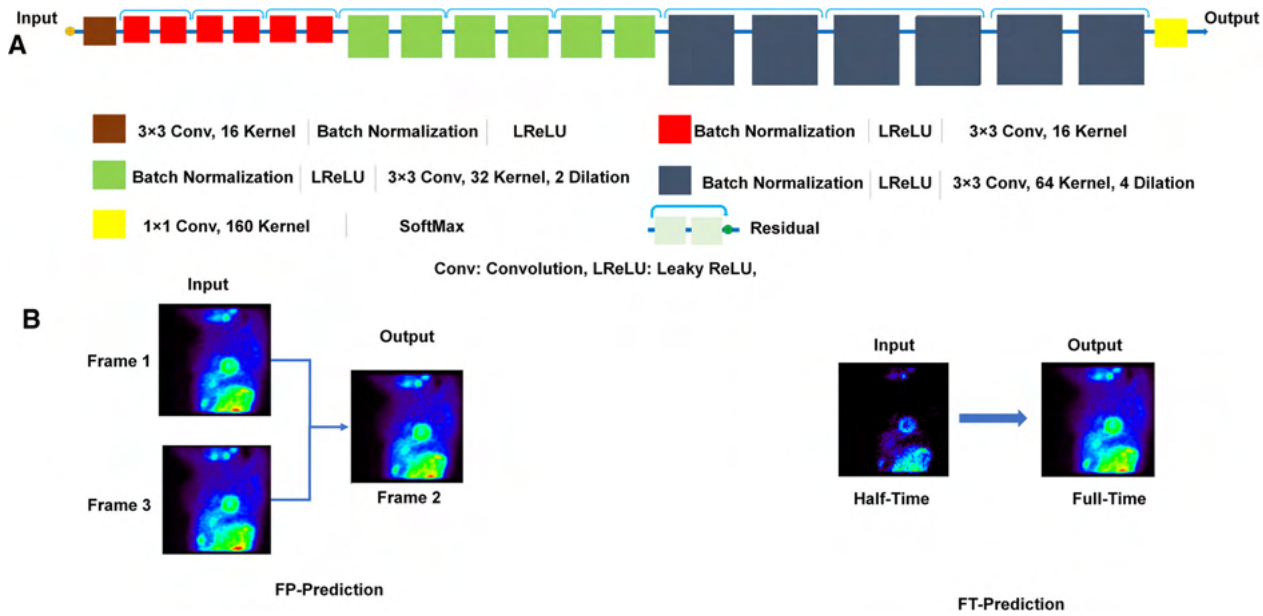

Figure 1. (**A**) Layout of the ResNet network architecture and details of the layers, (**B**) input and output of different scanning time reduction strategies. Red color layer: layer with dilation 1, green color layer: layer with dilation 2, blue color layer: layer with dilation 4. *Conv*, convolutional Kernel; *LReLu*, leaky rectified linear unit; *SoftMax*, Softmax function; *Residual*, residual connection; *FP-Prediction*, full projection prediction; *FT-Prediction*, full time prediction.

Table 1. Quantitative analysis of the predicted images in the projection domain relative to FT and FP scans

Method	ME (counts)	MAE (counts)	RE (%)	ARE (%)	SSIM	PSNR	RMSE (counts)
HT	− 37.6 ± 5.6	37.7 ± 5.1	− 23.1 ± 4.6	23.3 ± 4.5	0.92 ± 1.4	31.9 ± 1.6	68.4 ± 3.8
Predicted FT	− 0.3 ± 3.6	6.3 ± 2.4	0.4 ± 4.1	9.2 ± 3.0	0.96 ± 1.2	35.6 ± 1.8	11.7 ± 2.9
Predicted FP	− 0.4 ± 3.8	12.2 ± 2.8	− 2.9 ± 4.8	11.8 ± 3.7	0.94 ± 1.5	34.9 ± 1.9	16.4 ± 3.2
P-value*	< .05	< .002	< .01	< .02	< .05	< .05	< .02

**P*-value between predicted FT projections and predicted FP projections
FT-FP, full time and full projection (reference images); *HP*, half projection; *HT*, half time; *FP-Prediction*, full projection prediction; *FT-Prediction*, full time prediction; *ME*, Mean Error; *MAE*, mean absolute error; *RE%*, relative error; *ARE%*, absolute relative error; *SSIM*, structural similarity index; PSNR, peak signal-to-noise ratio; *RMSE*, root mean square error

SS (%) and SSS shown in Figure 7 provide detailed information about the distribution of these indices. The box plots in Supplemental Figures 4 and 5 compare the defect, wall, extent, ECC, SI and volume calculated from the different SPECT images. Descriptive statistics of Bland–Altman analysis were presented in Table 5. The mean differences (95%CI) of TPD were 0.43 [0.34, 0.53], 0.31 [0.14, 0.49], 1.81 [1.04, 2.58] and 2.35 [1.25, 3.45] for PFT, PFP, HP, and HT, respectively. The repeatability coefficients (95% CI) were 0.54 [0.38, 0.71] and 1.03 [0.73, 1.33] for PFT and PFP and increased to 4.58 [3.25, 5.90] and 6.57 [4.68, 8.46] for HP and HT, respectively.

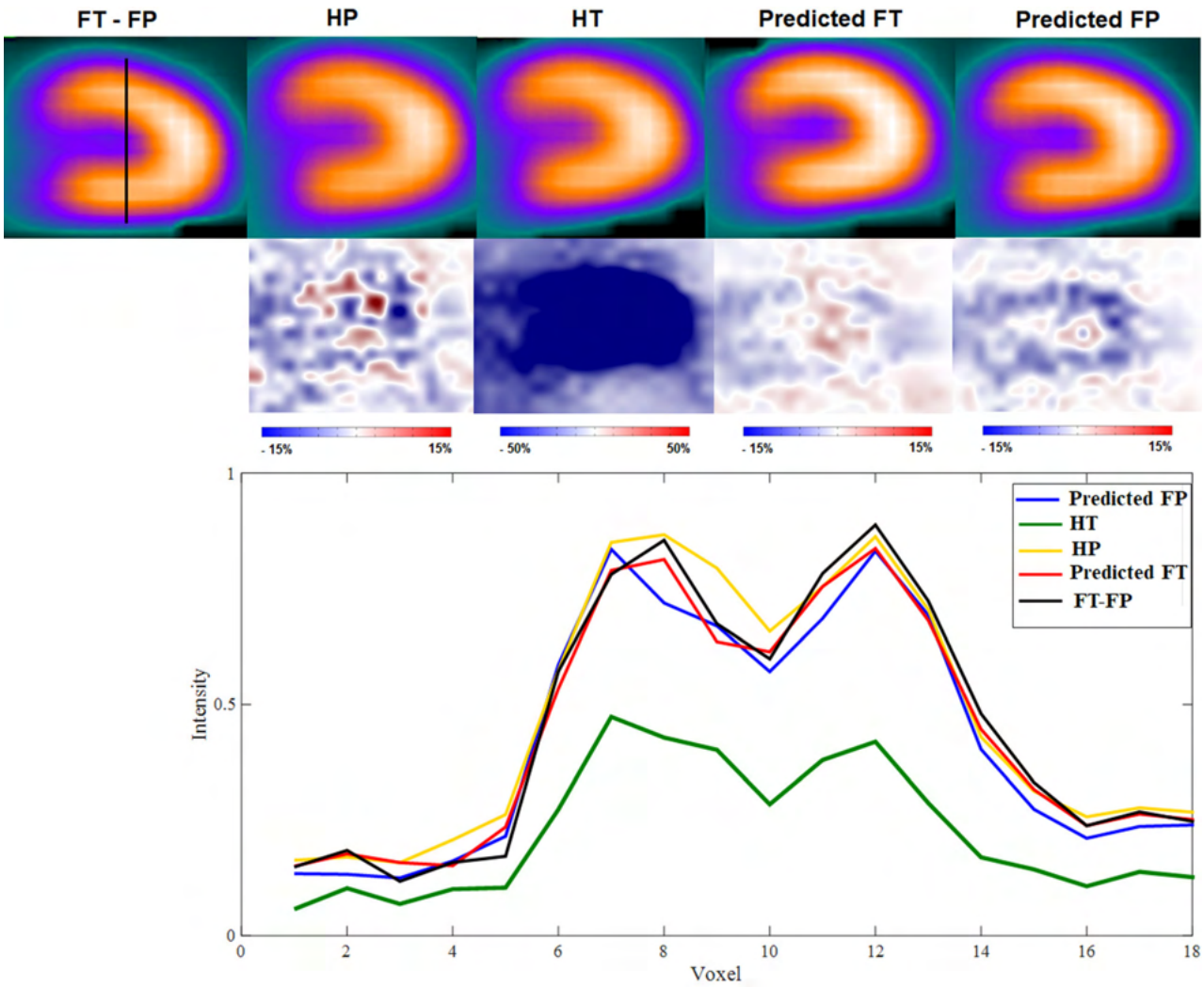

Figure 2. Representative MPI-SPECT clinical study showing FT-FP, predicted FT, predicted FP, HP and HT short-axis images, along with relative difference maps with respect to reference FT-FP images. Horizontal line profiles drawn through the myocardium are also shown. *FT-FP*, Full time full projection (reference images); *HP*, half projection; *HT*, half time; *FP-Prediction*, full projection prediction; *FT-Prediction*, full time prediction.

DISCUSSION

This study was set out with the aim of assessing the potential of half time MPI-SPECT imaging through two main approaches, namely reducing the number of projections and reducing the acquisition time per projection. The results demonstrated that HP reconstructed images produced better image quality compared to the HT reconstructed images. Moreover, the predicted FT images had better image quality than the predicted FP images. Among the generated images, the predicted FT images resulted in the lowest error metrics (RMSE = 6.8 ± 2.7, ARE = 3.1 ± 1.1%) and highest similarity index (SSIM = 0.97 ± 1.1, PSNR = 36.0 ± 1.4). The highest error metrics (RMSE = 32.8 ± 12.8, ARE = 16.2 ± 4.9%) and the lowest similarity (SSIM = 0.93 ± 2.6, PSNR = 31.7 ± 2.9) were observed in HT

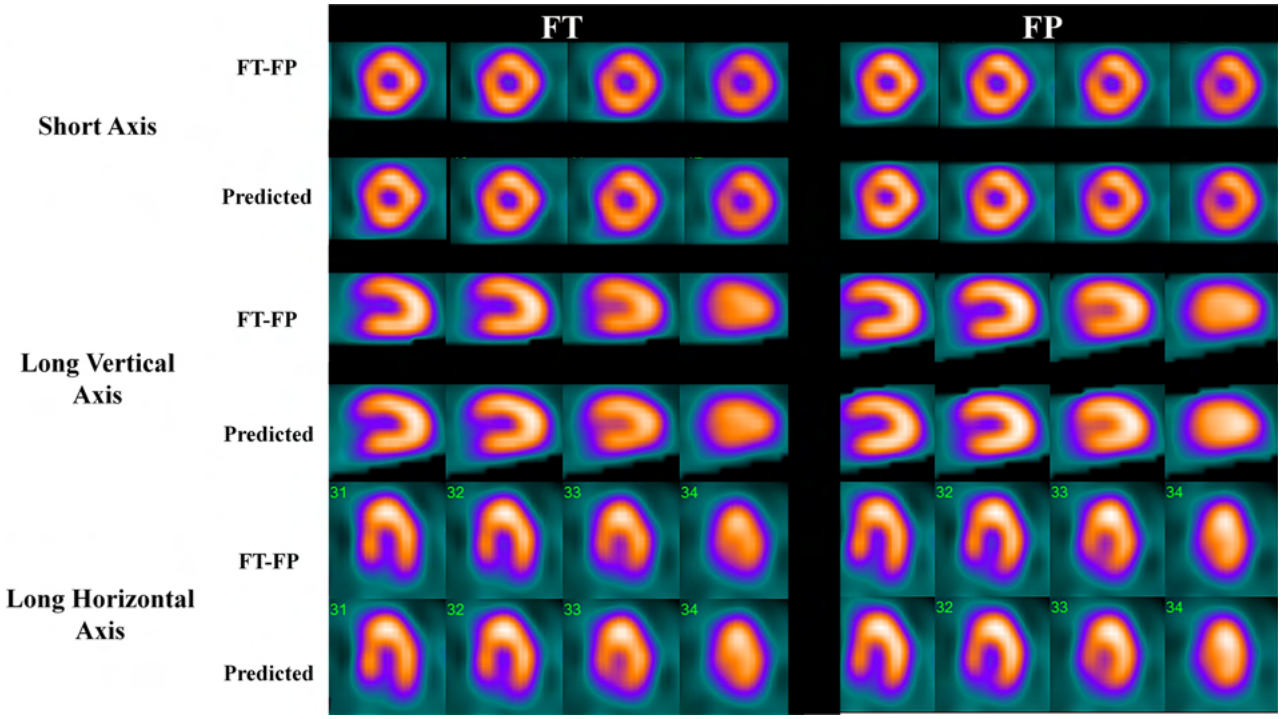

Figure 3. Representative MPI-SPECT clinical study showing FT-FP and predicted FP and predicted FT images. *FT-FP*, full time and full projection (reference images); *FP-Prediction*, full projection prediction; *FT-Prediction*, full time prediction.

images. The RMSE decreased significantly for predicted FT images (8.0 ± 3.6) relative to predicted FP images (6.8 ± 2.7) (P-value < .05).

Although the ProSPECT scanner used in this work, designed and built by our group, is not yet commercially available in many countries, its technical performance exhibited comparable performance in terms of sensitivity, spatial and energy resolution to other commercially available SPECT cameras.[25] Moreover, this study was conducted to investigate the potential of a novel deep learning-based low-dose/fast cardiac SPECT imaging, which is applicable on any SPECT camera offering sufficient flexibility for data acquisition. Hence, similar outcomes are expected when applying this approach on other commercial SPECT cameras.

A number of strategies were proposed for dose (half-dose or less than half-dose) and/or time (half-time or less than half- time) reduction in MPI-SPECT imaging.[29] Modern technologies, such as Cadmium-zinc telluride detectors[30] and IQ SPECT[6] were proposed for dose and time reduction, yet these specialized devices are not widely available and are still limited to few sites. Lecchi et al.[31] investigated the possibility of acquisition time reduction to 50% and 25% of the standard time on a general-purpose SPECT camera (BrightView, Philips Healthcare) using latest generation iterative reconstruction algorithms with resolution recovery (Astonish™ algorithm, Philips Healthcare). They reported significant (P-value < .01) detrimental influence on cardiac quantification in overweight patients when using 50% and 25% of standard acquisition time, though the approach is applicable in normal-weighted patients. In our study, decreasing the acquisition time to 50% of the standard time had a noticeable effect on quantitative parameters (RE = − 25.5 ± 9.1%). Application of the deep learning approach to produce predicted FT images decreased significantly (P-value < .001) the quantification errors (RE = − 0.2 ± 1.1%) compared to the FP/FT images used as reference. This study confirmed that decreasing the acquisition time significantly affected the derived

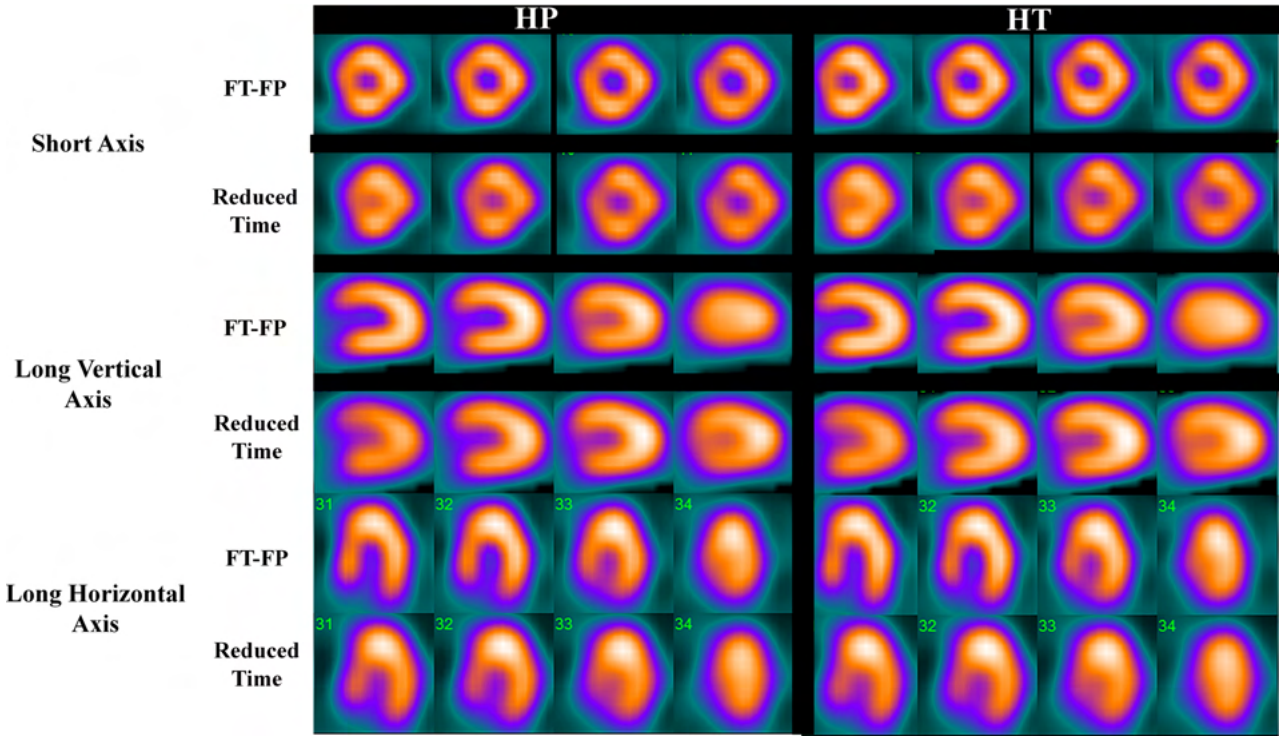

Figure 4. Representative MPI-SPECT clinical study showing FT-FP, HT and HP images. *FT-FP*, full time and full projection (Reference images); *HP*, half projection; *HT*, half time.

quantitative metrics, which can be recovered by the deep learning techniques.

The clinical evaluation revealed that the predicted FP and FT SPECT images reflect clinically relevant information in the reference FP/FT SPECT images with high accuracy. For instance, the predicted FT and FP images resulted in TPD% of 18.40% and 18.52%, respectively, compared to the reference FP/FT (TPD = 18.84%). Due to the increased noise levels in the projections and its adverse impact on the SPECT reconstruction, HT SPECT images exhibited noticeable loss of relevant information leading to TPD = 16.49%. In this regard, HP SPECT images showed closer similarity to the reference FT/FP SPECT images as noise levels in the projection space remained unchanged. The degradation of image quality in HP SPECT images was due to the reduced number of angular samples which impacted the outcome of image reconstruction from the limited number of projections.

Caobelli et al.[32] reported on the feasibility of 1/8th time MPI-SPECT imaging using the IQ SPECT camera. The results were statistically comparable to 1/4th time protocol using the IQ SPECT system. Regarding the application of the deep neural networks in low-dose SPECT imaging, Ramon et al.[23] applied a 3D convolutional neural network based on stacked convolutional auto-encoders for denoising low-dose (1/8th and 1/16th of clinical standard dose) MPI-SPECT images. They reported correlation coefficients of 0.96 (1/16th dose), 0.97 (predicted full dose from 1/16th), 0.97 (1/8th dose) and 0.98 (predicted full dose form 1/8th), with respect to full dose OSEM reconstructed images. The authors reported improved correlation coefficients between the predicted full dose from 1/8th dose with respect to 1/16th dose images (P-value $< .01$). In our work, the correlation coefficient between HT images (0.650) was significantly improved (0.987) by FT prediction using the deep learning approach (P-value $< .01$). The correlation between HP and FP images improved from 0.970 to 0.983 using FP prediction technique. These results confirm the high correlation between predicted images and FT/FP images.

Song et al.[24] reported on a low-dose (25% dose) denoising approach for cardiac-gated SPECT images using a 3D convolutional residual network. The authors compared their proposed predicted images with standard

Table 2. Quantitative analysis of the predicted images in the image domain relative to FT and FP images

Methods	ME (counts)	MAE (counts)	RE (%)	ARE (%)	SSIM	PSNR	RMSE (counts)
Predicted FP[1]	− 0.3 ± 1.6	5.6 ± 2.3	− 0.1 ± 1.0	3.6 ± 1.3	0.98 ± 1.1	36.8 ± 1.5	8.0 ± 3.6
HT[2]	− 25.5 ± 9.1	25.5 ± 9.1	− 16.2 ± 4.9	16.2 ± 4.9	0.93 ± 1.3	32.2 ± 1.5	32.8 ± 12.8
Predicted FT[3]	− 0.2 ± 1.1	4.8 ± 1.8	− 0.2 ± 0.7	3.1 ± 1.1	0.97 ± 1.1	36.0 ± 1.4	6.8 ± 2.7
HP[4]	0.1 ± 2.0	7.4 ± 2.8	0.1 ± 1.3	4.8 ± 1.7	0.96 ± 1.2	35.7 ± 1.5	10.7 ± 4.5
P-value (1 to 2)	.05	< .05	.07	< .05	< .05	< .05	< .05
P-value (1 to 3)	.09	< .05	.08	.05	.06	.06	< .05
P-value (1 to 4)	< .01	< .01	< .001	< .01	< .02	< .02	< .002
P-value (2 to 4)	< .001	< .001	< .001	< .001	< .001	< .001	< .001
P-value (2 to 3)	.07	< .05	.08	.05	.08	.09	< .05
P-value (3 to 4)	< .005	< .005	< .001	< .005	< .005	< .005	< .001

The *P*-values were calculated between the methods indicated by their numbers (from 1 to 4)
FT-FP, full time and full projection (Reference images); *HP*, half projection; *HT*, half time; *FP-Prediction*, full projection prediction; *FT-Prediction*, full time prediction; *ME*, mean error; *MAE*, mean absolute error; *RE%*, *ARE%*, absolute relative error; *SSIM*, structural similarity index; *PSNR*, peak signal-to-noise ratio; *RMSE,* root mean square error

dose and Gaussian post-filtering showing a reduction of the normalized MSE (NMSE) by 6.13% and 11.05%, respectively. They concluded that their proposed CNN method can yield marked improvements in denoising and resolution of SPECT images. In our proposed approach, the predicted FT images reduced the RMSE by 79.27% relative to HT images whereas the predicted FP reduced the RMSE by 25.23% compared to HP images. Kortelainen et al.[33] reported that image acquisition time of MPI-SPECT imaging can be reduced to half of standard imaging without significantly affecting the left ventricle volume, yet with significant deleterious effect on phase analysis. In our study, the HT images produced the highest RMSE, which was efficiently reduced by the deep learning approach.

Asao et al.[34] increased the number of projections using interpolation. They reported 2.07 ± 1.24% NMSE when using half projections, which significantly decreased to 1.85 ± 1.06% using the interpolation method. Sparse-view CT sinogram synthesis,[35] PET sinogram repair to mitigate detector block detectors,[36] partial-ring image restoration[37] or sinogram gap filling[38] were previously addressed using deep neural networks. In the present study, we aimed to reduce the number of projections by exploiting the sparse view concept taking advantage of the fact that iterative reconstruction reduces the sparse view effect. HP images resulted in a RMSE of 10.7 ± 4.5 with respect to FT/FP images using OSEM reconstruction algorithm. This was reduced to 8.0 ± 3.6 using the FP prediction technique (*P*-value < .05). The predicted FT and predicted FP images didn't show significant differences for most quantitative evaluation metrics. Yet, both methods provided more accurate quantification with respect to HT and HP images.

In this work, we included patients with various demographics, such as age, gender, and weight, and different clinical indications (normal, ischemia, and

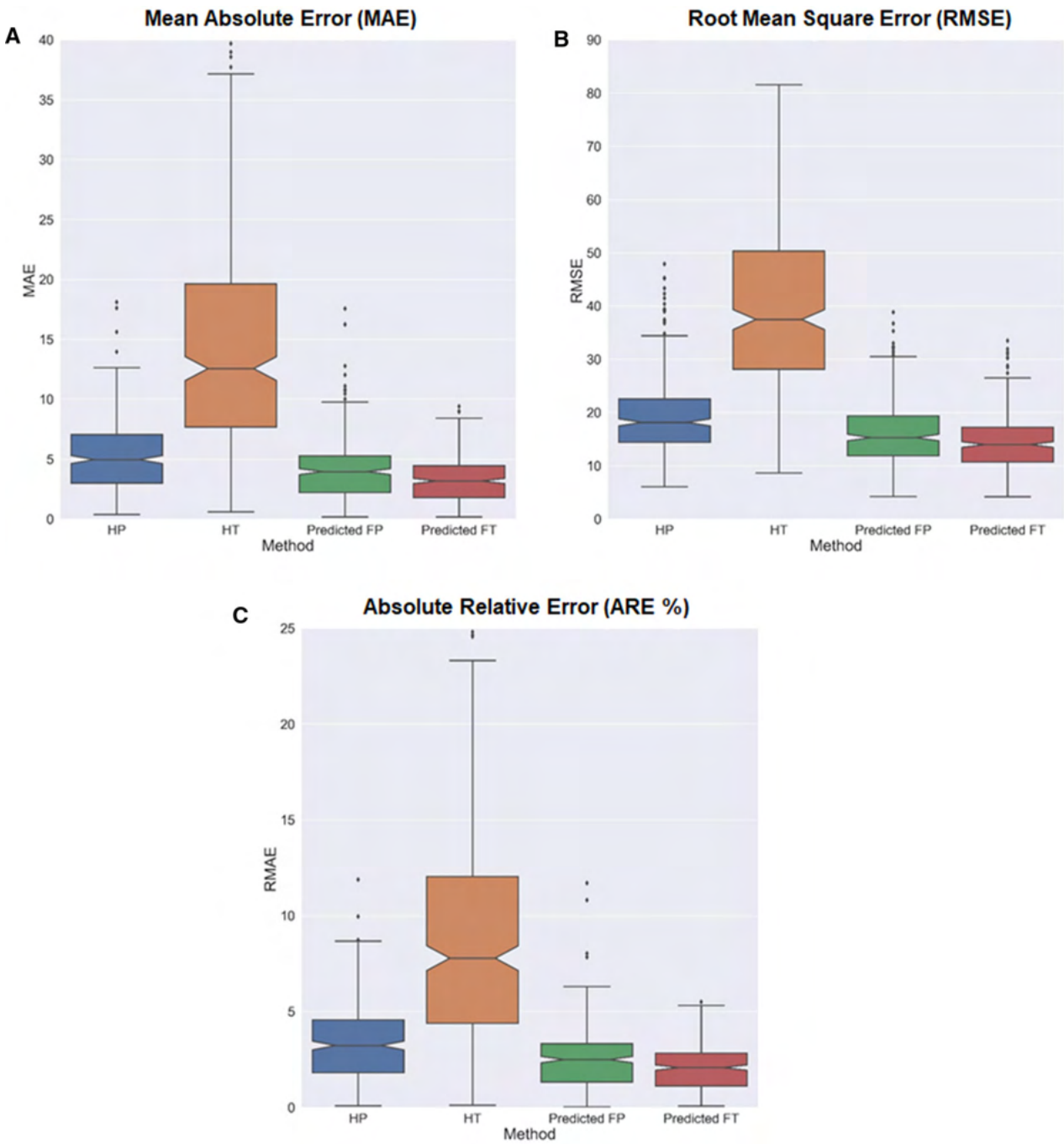

Figure 5. Box plots comparing various quantitative imaging metrics, including (**A**) MAE, (**B**) RMSE, and (**C**) ARE (%) for the various MPI-SPECT images. *MAE*, Mean absolute error; *RMSE*, root mean square error; *ARE (%)*, absolute relative error.

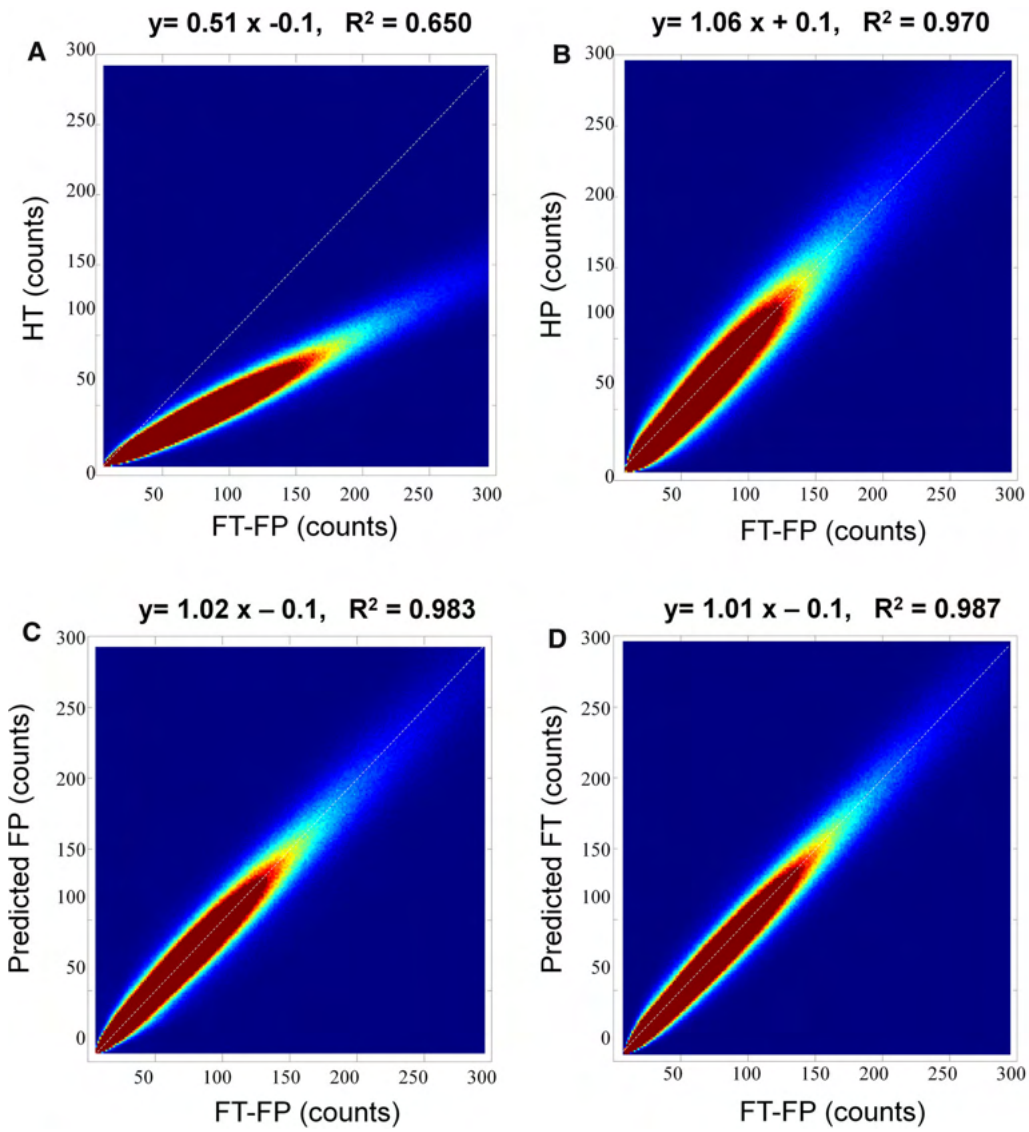

Figure 6. Voxelwise joint correlation histogram analysis of: (**A**) HT, (**B**) HP, (**C**) predicted FP and (**D**) predicted FT images vs FT-FP images. *FT-FP*, full time and full projection (reference images); *HP*, half projection; *HT*, half time; *FP-Prediction*, full projection prediction; *FT-Prediction*, full time prediction.

Table 3. Descriptive statistic of quantitative stress perfusion MPI of different image using Cedars-Sinai software

Parameters images		Minimum	Maximum	Mean	Std. deviation
Defect	FT-FP	4	31	20.78	7.54
	PFT	3	30	20.10	7.35
	PFP	4	30	20.06	7.24
	HP	6	26	17.49	5.84
	HT	0	25	16.54	5.75
Extent	FT-FP	4	41	25.47	9.16
	PFT	3	40	24.63	9.04
	PFP	4	40	24.32	8.78
	HP	6	33	21.33	7.27
	HT	0	33	20.65	7.30
Summed stress percent (SS %)	FT-FP	4	37	20.87	7.48
	PFT	4	37	20.40	7.08
	PFP	4	36	20.56	6.91
	HP	3	30	17.81	7.19
	HT	3	30	17.60	6.15
Summed stress score (SSS)	FT-FP	3	27	15.36	5.50
	PFT	3	27	15.04	5.25
	PFP	3	26	15.16	5.14
	HP	2	23	13.18	5.08
	HT	2	24	13.12	4.49
Total perfusion deficit (TPD %)	FT-FP	4	29	18.84	6.08
	PFT	4	29	18.40	6.00
	PFP	4	28	18.52	6.00
	HP	5	26	17.02	4.98
	HT	2	25	16.49	4.74
Volume	FT-FP	12	35	22.15	6.11
	PFT	12	35	22.09	6.05
	PFP	12	35	21.94	6.00
	HP	12	36	22.26	6.14
	HT	11	36	21.47	5.82
Wall	FT-FP	62	104	83.81	12.53
	PFT	62	104	83.77	12.30
	PFP	62	103	83.43	12.27
	HP	63	102	82.79	11.83
	HT	60	109	81.92	11.96
Shape eccentricity	FT-FP	0.64	0.97	0.81	0.09
	PFT	0.64	0.97	0.81	0.09
	PFP	0.63	0.97	0.81	0.09
	HP	0.66	0.93	0.79	0.07
	HT	0.63	0.99	0.77	0.08
Shape index	FT-FP	0.48	0.92	0.72	0.11
	PFT	0.48	0.92	0.72	0.11
	PFP	0.48	0.91	0.72	0.11
	HP	0.47	0.84	0.69	0.08
	HT	0.39	0.84	0.70	0.10

FT-FP, full time and full projection (reference images); *HP,* half projection; *HT*, half time; *FP-Prediction*, full projection prediction; *FT-Prediction*, full time prediction

Table 4. Pearson correlation (R^2) of different quantitative parameters with respect to reference images (FT-FP)

	Pearson correlation coefficient (R^2)			
Parameters	**PFT**	**PFP**	**HP**	**HT**
Defect	0.998	0.998	0.927	0.882
Extent	0.999	0.998	0.943	0.852
Summed stress percent (SS %)	0.993	0.991	0.641	0.681
Summed stress score (SSS)	0.994	0.992	0.678	0.72
Total perfusion deficit (TPD %)	0.999	0.996	0.93	0.837
Volume	1	0.999	0.975	0.796
Wall	0.999	0.999	0.94	0.673
Shape eccentricity	1.0	1.0	0.937	0.849
Shape index	0.999	0.999	0.879	0.660

HP, half projection; *HT*, half time; *FP-Prediction*, full projection prediction; *FT-Prediction*, full time prediction

infarct) resulting in a heterogeneous clinical cohort. One of the more significant findings of this study is the potential of acquisition time reduction in MPI-SPECT imaging using deep learning methods, which can be easily implemented on any SPECT camera and data acquisition protocol. The generalizability of these results is subject to certain limitations. Among the limitations of this study is that image processing and analysis was performed on non-gated static images and such, further research should focus on gated MPI-SPECT images. Being limited to non-gated MPI-SPECT, this study lacks typical cardiac quantitative SPECT analysis, such as quantitative gated SPECT (QGS) analysis. Future studies need to be carried out to validate the proposed methodology for the extraction of MPI-SPECT cardiac quantification metrics and features. Notwithstanding these limitations, the study suggests the feasibility of acquisition time reduction using a deep residual neural network, which can easily be extended to gated MPI-SPECT imaging.

CONCLUSION

We assessed the feasibility of acquisition time reduction in MPI-SPECT imaging using deep learning through two main approaches, reduction of acquisition time per projection and reduction of the number of angular projections. It was concluded that reducing the acquisition time per projection deteriorates image quality and increases quantification errors that are efficiently recovered using the deep neural network algorithm. Further reduction in acquisition time might be possible through the use of more advanced neural networks.

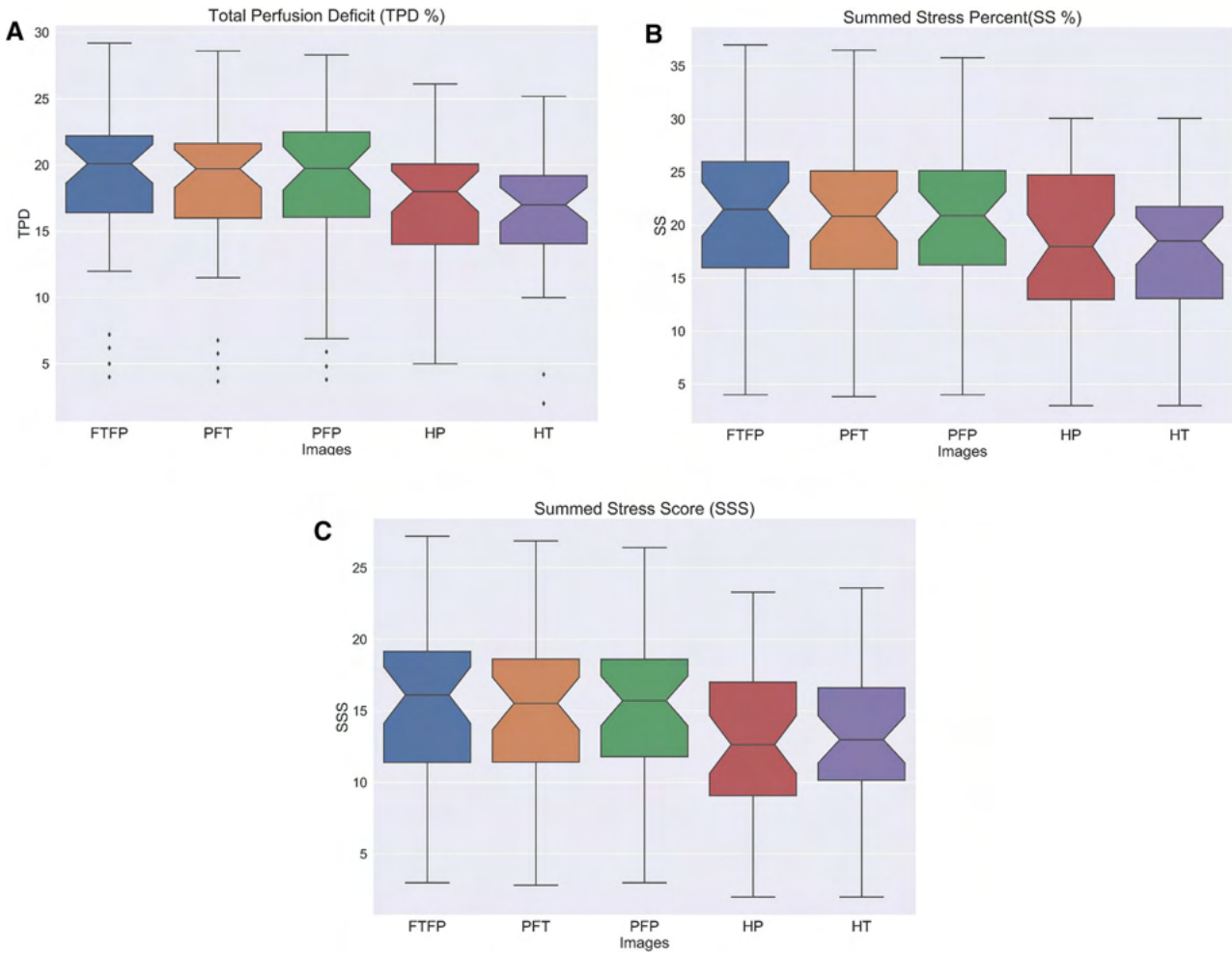

Figure 7. Clinical quantitative parameters including total perfusion deficit (TPD%), Summed stress percent (SS%) and Summed stress score (SSS) in different images. *FT-FP*, full time and full projection (reference images); *HP*, half projection; *HT*, half- time; *FP-Prediction*, full projection prediction; *FT-Prediction*, full time prediction.

Table 5. Descriptive statistics of Bland-Altman analysis of quantitative stress perfusion MPI of different image using Cedars-Sinai software

Parameters	Feature	Bias (mean) Diff [95% CI]	Bias STD	Lower LOA [95% CI]	Upper LOA [95% CI]	RC [95% CI]
Defect	PFT	0.68 [0.53, 0.83]	0.46	− 0.22 [− 0.48, 0.04]	1.59 [1.33, 1.85]	0.90 [0.64, 1.16]
	PFP	0.72 [0.53, 0.91]	0.57	− 0.39 [− 0.72, − 0.07]	1.85 [1.53, 2.18]	1.13 [0.81, 1.46]
	HP	3.29 [2.29, 4.29]	3.05	− 2.69 [− 4.41, − 0.95]	9.26 [7.54, 11.00]	5.97 [4.25, 7.71]
	HT	4.24 [3.03, 5.44]	3.66	− 2.95 [− 5.02, − 0.86]	11.40 [9.34, 13.5]	7.18 [5.12, 9.28]
Extent	PFT	0.83 [0.70, 0.96]	0.39	0.05 [− 0.17, 0.27]	1.62 [1.39, 1.84]	0.78 [0.55, 1.00]
	PFP	0.80 [0.61, 0.98]	0.57	− 0.32 [− 0.64, 0.00]	1.92 [1.60, 2.25]	1.12 [0.80, 1.45]
	HP	4.13 [3.03, 5.23]	3.35	− 2.43 [− 4.32, − 0.53]	10.7 [8.79, 12.60]	6.56 [4.65, 8.46]
	HT	4.82 [3.23, 6.40]	4.83	− 4.64 [− 7.38, − 1.91]	14.3 [11.5, 17.00]	9.46 [6.66, 12.16]
Summed Stress Percent (SS %)	PFT	0.46 [0.15, 0.77]	0.93	− 1.36 [− 1.89, − 0.83]	2.29 [1.76, 2.82]	1.83 [1.30, 2.36]
	PFP	0.30 [− 0.06, 0.67]	1.13	− 1.91 [− 2.56, − 1.27]	2.52 [1.88, 3.17]	2.22 [1.58, 2.87]
	HP	3.06 [1.01, 5.11]	6.22	− 9.14 [− 12.70, − 5.61]	15.3 [11.70, 18.80]	12.20 [8.60, 15.70]
	HT	3.27 [1.44, 5.11]	5.58	− 7.67 [− 10.80, − 4.51]	14.2 [11.00, 17.40]	10.90 [7.70, 14.10]
Summed Stress Score (SSS)	PFT	0.32 [0.12, 0.52]	0.62	− 0.89 [− 1.24, − 0.54]	1.54 [1.19, 1.89]	1.22 [0.87, 1.57]
	PFP	0.20 [− 0.05, 0.45]	0.76	− 1.29 [− 1.72, − 0.86]	1.69 [1.26, 2.12]	1.49 [1.06, 1.92]
	HP	2.19 [0.78, 3.59]	4.27	− 6.18 [− 8.59, − 3.76]	10.5 [8.13, 13.00]	8.36 [5.99, 10.86]
	HT	2.25 [0.97, 3.52]	3.86	− 5.32 [− 7.50, − 3.13]	9.81 [7.62, 12.00]	7.56 [5.37, 9.75]
Total Perfusion Deficit (TPD %)	PFT	0.43 [0.34, 0.53]	0.27	− 0.10 [− 0.26, 0.05]	0.98 [0.82, 1.15]	0.54 [0.38, 0.71]
	PFP	0.31 [0.14, 0.49]	0.52	− 0.71 [− 1.01, − 0.41]	1.35 [1.05, 1.65]	1.03 [0.73, 1.33]
	HP	1.81 [1.04, 2.58]	2.34	− 2.77 [− 4.09, − 1.44]	6.40 [5.07, 7.72]	4.58 [3.25, 5.90]
	HT	2.35 [1.25, 3.45]	3.35	− 4.22 [− 6.12, − 2.3]	8.91 [7.02, 0.8]	6.57 [4.68, 8.46]
Volume	PFT	0.06 [0.00, 0.11]	0.16	− 0.26 [− 0.36, − 0.17]	0.39 [0.29, 0.48]	0.33 [0.23, 0.42]
	PFP	0.21 [0.13, 0.29]	0.24	− 0.27 [− 0.41, − 0.13]	0.70 [0.55, 0.84]	0.48 [0.34, 0.62]
	HP	− 0.11 [− 0.56, 0.33]	1.37	− 2.79 [− 3.56, − 2.01]	2.57 [1.79, 3.34]	2.68 [1.90, 3.45]
	HT	0.68 [− 0.57, 1.94]	3.82	− 6.81 [− 8.97, − 4.64]	8.17 [6.01, 10.3]	7.49 [5.33, 9.62]
Wall	PFT	0.04 [− 0.10, 0.19]	0.45	− 0.85 [− 1.11, − 0.59]	0.94 [0.68, 1.20]	0.89 [0.63, 1.15]
	PFP	0.38 [0.19, 0.57]	0.58	− 0.75 [− 1.09, − 0.42]	1.52 [1.19, 1.85]	1.14 [0.81, 1.47]
	HP	1.02 [− 0.38, 2.42]	4.26	− 7.33 [− 9.75, − 4.92]	9.37 [6.96, 11.80]	8.35 [5.94, 10.78]
	HT	1.89 [− 1.37, 5.15]	9.91	− 17.5 [− 23.1, − 11.9]	21.3 [15.7, 26.90]	19.4 [13.8, 25.00]

Table 5 continued

Parameters	Feature	Bias (mean) Diff [95% CI]	Bias STD	Lower LOA [95% CI]	Upper LOA [95% CI]	RC [95% CI]
Shape Eccentricity	PFT	0.000 [0.000, 0.001]	0.002	− 0.003 [− 0.004, − 0.002]	0.005 [0.003, 0.006]	0.004 [0.003, 0.005]
	PFP	0.002 [0.001, 0.003]	0.002	− 0.003 [− 0.004, − 0.001]	0.007 [0.006, 0.009]	0.005 [0.003, 0.006]
	HP	0.019 [0.007, 0.031]	0.036	− 0.051 [− 0.071, − 0.030]	0.090 [0.070, 0.111]	0.071 [0.050, 0.091]
	HT	0.035 [0.018, 0.051]	0.049	− 0.062 [− 0.090, − 0.034]	0.132 [0.104, 0.161]	0.097 [0.060, 0.126]
Shape Index	PFT	0.000 [− 0.001, 0.002]	0.005	− 0.010 [− 0.013, − 0.007]	0.011 [0.008, 0.014]	0.011 [0.007, 0.014]
	PFP	− 0.001 [− 0.003, 0.001]	0.005	− 0.011 [− 0.014, − 0.008]	0.008 [0.005, 0.011]	0.010 [0.007, 0.013]
	HP	0.021 [0.004, 0.039]	0.052	− 0.081 [− 0.111, − 0.051]	0.125 [0.094, 0.154]	0.103 [0.072, 0.132]
	HT	0.016 [− 0.011, 0.044]	0.084	− 0.149 [− 0.197, − 0.101]	0.182 [0.134, 0.230]	0.166 [0.118, 0.214]

FT-FP, full time and full projection (reference images); *HP*, half projection; *HT*, half time; *FP-Prediction*, Full projection prediction; *FT-Prediction*, full time prediction

Acknowledgments

This work was supported by the Swiss National Science Foundation under Grant SNRF 320030_176052.

Disclosure

There is no conflict of interest.

References

1. Iskandrian AE, Garcia EV. Nuclear cardiac imaging: Principles and applications. Oxford: Oxford University Press; 2008.
2. Rahmim A, Zaidi H. PET versus SPECT: Strengths, limitations and challenges. Nucl Med Commun 2008;29:193-207.
3. Wu J, Liu C. Recent advances in cardiac SPECT instrumentation and imaging methods. Phys Med Biol 2019;64:06TR1.
4. Ljungberg M, Pretorius PH. SPECT/CT: An update on technological developments and clinical applications. Br J Radiol 2018;91:20160402.
5. Rahmim A, Qi J, Sossi V. Resolution modeling in PET imaging: Theory, practice, benefits, and pitfalls. Med Phys 2013;40:064301-15.
6. Caobelli F, Kaiser SR, Thackeray JT, Bengel FM, Chieregato M, Soffientini A, et al. IQ SPECT allows a significant reduction in administered dose and acquisition time for myocardial perfusion imaging: Evidence from a phantom study. J Nucl Med 2014;55:2064-70.
7. Valenta I, Treyer V, Husmann L, Gaemperli O, Schindler MJ, Herzog BA, et al. New reconstruction algorithm allows shortened acquisition time for myocardial perfusion SPECT. Eur J Nucl Med Mol Imaging 2010;37:750-7.
8. DePuey EG, Bommireddipalli S, Clark J, Thompson L, Srour Y. Wide beam reconstruction ''quarter-time'' gated myocardial perfusion SPECT functional imaging: A comparison to ''full-time'' ordered subset expectation maximum. J Nucl Cardiol 2009;16:736-52.
9. Faes L, Wagner SK, Fu DJ, Liu X, Korot E, Ledsam JR, et al. Automated deep learning design for medical image classification by health-care professionals with no coding experience: A feasibility study. Lancet Digit Health 2019;1:e232-42.
10. Ding Y, Sohn JH, Kawczynski MG, Trivedi H, Harnish R, Jenkins NW, et al. A deep learning model to predict a diagnosis of Alzheimer disease by using (18)F-FDG PET of the brain. Radiology 2019;290:456-64.
11. Sanaat A, Arabi H, Mainta I, Garibotto V, Zaidi H. Projection-space implementation of deep learning-guided low-dose brain PET imaging improves performance over implementation in image-space. J Nucl Med 2020 (in press).
12. Shiri I, Leung K, Ghafarian P, Geramifar P, Oveisi M, Ay MR, et al. HiResPET: High resolution PET image generation using deep convolution encoder decoder network [abstract]. J Nucl Med 2019;60:1368.
13. Zhu B, Liu JZ, Cauley SF, Rosen BR, Rosen MS. Image reconstruction by domain-transform manifold learning. Nature 2018;555:487-92.
14. Zhong Z, Kim Y, Plichta K, Allen BG, Zhou L, Buatti J, et al. Simultaneous cosegmentation of tumors in PET-CT images using deep fully convolutional networks. Med Phys 2019;46:619-33.
15. Xie T, Zaidi H. Estimation of the radiation dose in pregnancy: An automated patient-specific model using convolutional neural networks. Eur Radiol 2019;29:6805-15.
16. Shiri I, Ghafarian P, Geramifar P, Leung KH, Ghelichoghli M, Oveisi M, et al. Direct attenuation correction of brain PET images using only emission data via a deep convolutional encoder-decoder (Deep-DAC). Eur Radiol 2019;29:6867–79.
17. Arabi H, Zeng G, Zheng G, Zaidi H. Novel adversarial semantic structure deep learning for MRI-guided attenuation correction in brain PET/MRI. Eur J Nucl Med Mol Imaging 2019;46:2746-59.
18. Ma L, Ma C, Liu Y, Wang X. Thyroid diagnosis from SPECT images using convolutional neural network with optimization. Comput Intell Neurosci 2019;2019:6212759.
19. Betancur J, Commandeur F, Motlagh M, Sharir T, Einstein AJ, Bokhari S, et al. Deep learning for prediction of obstructive disease from fast myocardial perfusion SPECT: A multicenter study. JACC Cardiovasc Imaging 2018;11:1654-63.
20. Betancur J, Hu L-H, Commandeur F, Sharir T, Einstein AJ, Fish MB, et al. Deep learning analysis of upright-supine high-efficiency spect myocardial perfusion imaging for prediction of obstructive coronary artery disease: A multicenter study. J Nucl Med 2019;60:664-70.
21. Wang T, Lei Y, Tang H, He Z, Castillo R, Wang C, et al. A learning-based automatic segmentation and quantification method on left ventricle in gated myocardial perfusion SPECT imaging: A feasibility study. J Nucl Cardiol 2019. https://doi.org/10.1007/s12350-019-01594-2.
22. Dietze MM, Branderhorst W, Kunnen B, Viergever MA, de Jong HW. Accelerated SPECT image reconstruction with FBP and an image enhancement convolutional neural network. EJNMMI Phys 2019;6:14.
23. Ramon AJ, Yang Y, Pretorius PH, Johnson KL, King MA, Wernick MN. Initial investigation of low-dose spect-MPI via deep learning. 2018 IEEE Nuclear Science Symposium and Medical Imaging Conference Proceedings (NSS/MIC); 2018. p. 1-3.
24. Song C, Yang Y, Wernick MN, Pretorius PH, King MA. Low-dose cardiac-gated spect studies using a residual convolutional neural network. 2019 IEEE 16th International Symposium on Biomedical Imaging (ISBI 2019); 2019. p. 653-6.
25. Zeraatkar N, Sajedi S, Fard BT, Kaviani S, Akbarzadeh A, Farahani M, et al. Development and calibration of a new gamma camera detector using large square photomultiplier tubes. J Instrum 2017;12:P09008.
26. Li W, Wang G, Fidon L, Ourselin S, Cardoso MJ, Vercauteren T. On the compactness, efficiency, and representation of 3D convolutional networks: Brain parcellation as a pretext task. International Conference on Information Processing in Medical Imaging; 2017. p. 348-60.
27. Gibson E, Li W, Sudre C, Fidon L, Shakir DI, Wang G, et al. NiftyNet: A deep-learning platform for medical imaging. Comput Methods Programs Biomed 2018;158:113-22.
28. Abadi M, Barham P, Chen J, Chen Z, Davis A, Dean J et al. TensorFlow: A system for large-scale machine learning. Proceedings of the 12th USENIX conference on Operating Systems Design and Implementation. Savannah, GA, USA; 2016. p. 265-83.
29. Dorbala S, Blankstein R, Skali H, Park M-A, Fantony J, Mauceri C, et al. Approaches to reducing radiation dose from radionuclide myocardial perfusion imaging. J Nucl Med 2015;56:592-9.
30. Acampa W, Buechel RR, Gimelli A. Low dose in nuclear cardiology: State of the art in the era of new cadmium–zinc-telluride cameras. Eur Heart J Cardiovasc Imaging 2016;17:591-5.
31. Lecchi M, Martinelli I, Zoccarato O, Maioli C, Lucignani G, Del Sole A. Comparative analysis of full-time, half-time, and quarter-time myocardial ECG-gated SPECT quantification in normal-weight and overweight patients. J Nucl Cardiol 2017;24:876-87.

32. Caobelli F, Thackeray JT, Soffientini A, Bengel FM, Pizzocaro C, Guerra UP. Feasibility of one-eighth time gated myocardial perfusion SPECT functional imaging using IQ-SPECT. Eur J Nucl Med Mol Imaging 2015;42:1920-8.
33. Kortelainen MJ, Koivumäki TM, Vauhkonen MJ, Hakulinen MA. Dependence of left ventricular functional parameters on image acquisition time in cardiac-gated myocardial perfusion SPECT. J Nucl Cardiol 2015;22:643-51.
34. Asao K, Takaki A, Tominaga M, Sasaki M. The interpolated projection data estimation method improves the image quality of myocardial perfusion SPECT with a short acquisition time. Ann Nucl Med 2012;26:123-30.
35. Lee H, Lee J, Kim H, Cho B, Cho S. Deep-neural-network-based sinogram synthesis for sparse-view CT Image reconstruction. EEE Trans Radiat Plasma Med Sci 2018;3:109-19.
36. Deidda D, Karakatsanis NA, Robson PM, Efthimiou N, Fayad ZA, Aykroyd RG, et al. Effect of PET-MR inconsistency in the kernel image reconstruction method. IEEE Trans Rad Plasma Med Sci 2019;3:400-9.
37. Jonsson BA, Bjornsdottir G, Thorgeirsson TE, Ellingsen LM, Walters GB, Gudbjartsson DF, et al. Brain age prediction using deep learning uncovers associated sequence variants. Nat Commun 2019;10:5409.
38. Shiri I, Sheikhzadeh P, Ay MR. Deep-Fill: Deep learning based sinogram domain gap filling in positron emission tomography. 2019. arXiv:1906.07168.